Journal of Alloys and Compounds 513 (2012) 139–144

Contents lists available at SciVerse ScienceDirect

Journal of Alloys and Compounds

journal homepage: www.elsevier.com/locate/jallcom

Efficient down- and up-conversion of Pr^{3+}–Yb^{3+} co-doped transparent oxyfluoride glass ceramics

Q.J. Chen, W.J. Zhang, X.Y. Huang, G.P. Dong, M.Y. Peng, Q.Y. Zhang*

State Key Laboratory of Luminescent Materials and Devices and Institute of Optical Communication Materials, South China University of Technology, Guangzhou 510641, PR China

ARTICLE INFO

Article history:
Received 26 July 2011
Received in revised form 1 October 2011
Accepted 3 October 2011
Available online 17 October 2011

Keywords:
Up-conversion
Down-conversion
Glass ceramics
CaF_2 nanocrystals
Pr^{3+} ions

ABSTRACT

Pr^{3+} and/or Yb^{3+} doped transparent oxyfluoride glass ceramics (GCs) containing CaF_2 nanocrystals were fabricated and characterized by X-ray diffraction (XRD) and transmission electron microscopy (TEM). Judd–Ofelt (J–O) intensity parameters, radiative transition probability, radiative lifetimes, and branching ratios of Pr^{3+} have been calculated from the absorption spectra. Upon 470 nm excitation, Pr^{3+} doped GCs yield intense visible-near infrared (NIR) luminescence corresponding to the $^3P_0 \rightarrow {}^3H_6$, $^3P_0 \rightarrow {}^3F_{2,3,4}$, $^3P_1 \rightarrow {}^1G_4$, $^1D_2 \rightarrow {}^3H_5$, and $^1D_2 \rightarrow {}^3F_4$ transitions, respectively. With the addition of Yb^{3+} ions, NIR down-conversion (DC) emissions at 976 nm ($^2F_{5/2} \rightarrow {}^2F_{7/2}$) were achieved, due to efficient energy transfer (ET) from Pr^{3+} to Yb^{3+}. Underlying mechanism for the NIR-DC is analyzed in terms of static and dynamic photoemission and monitored excitation spectra. The maximum quantum efficiency from Pr^{3+}:$^3P_0$ to Yb^{3+}:$^2F_{5/2}$ is calculated to be 153%. In comparison, intense up-conversion emissions at 489, 545, 606, and 651 nm have been obtained in Pr^{3+}–Yb^{3+} codoped glass and GCs under 980 nm excitation, which is ascribed to be two-photon involved ET from Yb^{3+} to Pr^{3+}.

1. Introduction

The conversion from sunlight to electricity using solar cell devices represents a promising approach to green and renewable energy [1–4]. Despite relevant technology having been around for more than half a century, solar energy remains non-price-competitive with traditional fossil fuels, mainly owing to the low energy conversion efficiencies of solar cells. State-of-the-art commercial crystalline Si (*c*-Si) solar cells with operating energy efficiencies only around 15% dominate the present photovoltaic technologies [3]. Major energy loss in solar cells is due to the nature of the photovoltaic effect. The absorption of one incident high energy photon can generate a single electron–hole pair, with the excess energy being lost as heat [5]. Effective harvesting the energy from ultraviolet (UV) and blue photons is a necessary condition for enhancing the efficiencies of solar cells [6]. According to the terrestrial solar spectrum at air mass (AM) 1.5 depicted in Fig. 1(up) [7], spectrum modulation by converting the UV–visible photons into near-infrared (NIR) photons below the band gap of *c*-Si (1.12 eV) where *c*-Si solar cells exhibit their greatest spectral response, can enhance the energy conversion efficiencies of the *c*-Si solar cells [8]. Recently, the down-conversion (DC) process which is based on the principle of converting every incident UV-blue photon into at least two NIR photons, has been realized with the rare earth (RE) ion-pairs such as Tb^{3+}–Yb^{3+}, Tm^{3+}–Yb^{3+} and Pr^{3+}–Yb^{3+} [9–12]. The theoretical maximum quantum efficiency can reach nearly 200%. Therefore, these RE ions doped DC materials are expected to act as spectra converters and concentrators for *c*-Si solar cells [8,13–15].

The luminescence of most RE ions with small energy gaps in 4f shell are greatly influenced by the composition and structure of the host materials. Materials with lower vibrational energy, which can minimize the non-radiative transitions, are thus preferable for up-conversion (UC) and DC luminescence [16–18]. Oxyfluoride glass ceramics (GCs), which possess high transparency and the combined merits of stable physical and chemical performance of oxide glasses and the low phonon energy of fluoride crystals, were considered as the excellent host materials for UC and DC [19–24]. Compared to powder phosphors, RE ions doped DC GCs are more preferable to serve as spectrum conversion layer in front of the c-Si solar cells due to their higher transparency for visible and infrared sunlight. On the other hand, owing to the three successive energy levels of $^3P_{0,1,2}$, the Pr^{3+} ions possess a broad absorption band in the range of 420–500 nm, which is considered to be the suitable sensitizer for the Yb^{3+} ions.

Herein, we reported the efficient NIR emissions around 976 nm of Yb^{3+} ions from Pr^{3+}–Yb^{3+} codoped GCs via DC process under the excitation of 470 nm. The corresponding energy transfer (ET) mechanisms for Pr^{3+}–Pr^{3+} and Pr^{3+}–Yb^{3+} were analyzed. The UC luminescence of Pr^{3+}–Yb^{3+} was also investigated.

* Corresponding author. Tel.: +86 20 87113681; fax: +86 20 87114204.
E-mail address: qyzhang@scut.edu.cn (Q.Y. Zhang).

0925-8388/$ – see front matter © 2011 Elsevier B.V. All rights reserved.
doi:10.1016/j.jallcom.2011.10.007

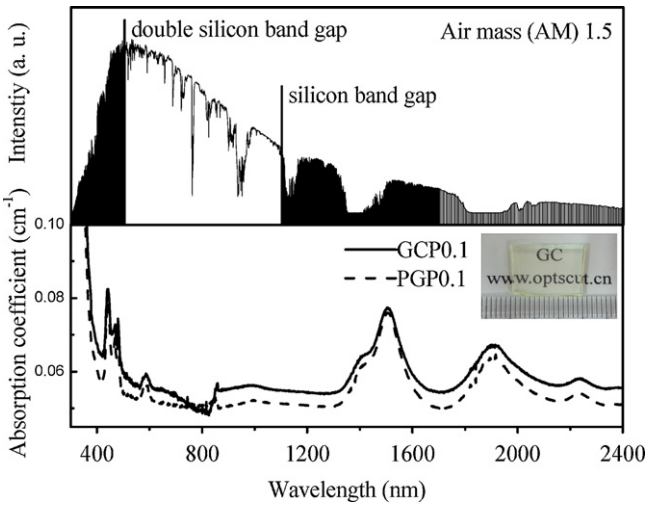

Fig. 1. The upper one is the terrestrial solar spectrum at air mass (AM) 1.5. Lower one shows absorption spectra of PGP0.1 and GCP0.1. Inset: photograph of transparent GCP0.1.

2. Experimental

Oxyfluoride glass samples with nominal molar compositions of $45SiO_2$–$25Al_2O_3$–$10Na_2O$–$20CaF_2$–$xPrF_3$ (denoted as PGPx) (x = 0.05, 0.1, 0.5, and 1), and $45SiO_2$–$25Al_2O_3$–$10Na_2O$–$20CaF_2$–$0.1PrF_3$–$YYbF_3$ (denoted as PGYy) (y = 0.1, 0.3, 0.5, 1.0 and 1.5) were prepared by melting mixtures of raw materials in covered corundum crucibles at 1450 °C for 1 h in air. The melts were then poured onto a preheated (200 °C) stainless steel plate and annealed at 450 °C for 2 h. The obtained glasses were heat-treated at 570 °C for 2 h to fabricate transparent GCPx and GCYy GC samples. The inset of Fig. 1(down) shows the photograph of GCP0.1. Oxyfluoride glass system SiO_2–Al_2O_3–Na_2O–CaF_2 have chosen as matrix material due to its advantages such as a good transparency in the visible to infrared (0.3–3 um), high mechanical properties, good glass stability and rare-earth ions solubility, and the crystallization of the glass ceramics easy to control as well.

Differential scanning calorimetry (DSC) measurement was carried out in a simultaneous thermal analyzer (STA449C NETZSCH) at the heating rate of 10 K/min to determine the glass transition (T_g) and crystallization (T_x) temperatures. To identify the crystallization phase, X-ray diffraction (XRD) measurements were performed on a Philips Model PW1830 diffractometer with a step size of 0.033 under Cu Kα radiation. Transmission electron microscope (TEM, JEM-2010) assembled with the selected area electron diffraction (SAED) were employed to analyze the microstructure of GC samples. The samples were firstly grinded in a burnisher with alcohol for about half an hour, and then more alcohol was added and the samples dispersed via ultrasonic oscillation. Finally, the samples, which dispersed in the liquid, were drop on a grid for TEM measurement. The absorption spectra were obtained from a Perkin-Elmer Lambda 900 UV/vis/NIR spectrophotometer in the spectral range of 300–2400 nm with the resolution of 1 nm. Photoluminescence (PL) and PL excitation (PLE) spectra of GC samples were measured using a Jobin-Yvon Triax 320 spectrometer equipped with Hamamatsu R5108 photomultiplier tube for NIR emission and R928 photomultiplier tube for visible emission under excitation of 470 nm tuned from a continuous wavelength xenon lamp (450 W). The decay curves were collected by a Tektronix TDS3012B digital phosphor oscilloscope. The UC luminescence measurements were performed on a Triax 320 spectrometer upon excitation of a 980 nm laser diode (LD). All the measurements were carried out at room temperature.

3. Results and discussion

3.1. Microstructure

Fig. 2(a) presents the DSC curve of the Pr^{3+} doped glass where T_g and T_x are found to be 550 and 666 °C, respectively. The XRD patterns of the precursor glass (PG) and GC samples are shown in Fig. 2(b). It is found that the PG is amorphous with only two diffuse humps. After thermal treatment at 570 °C for 2 h, the pattern consists of several intense diffraction peaks on the amorphous humps, which can be attributed to the crystallization of cubic CaF_2 phase (JCPDS Card No. 01-1274). Based on the Scherer formula, the mean size of CaF_2 nanocrystals was evaluated to be ~11 nm. The TEM micrograph presented in Fig. 2(c) indicates that nanocrystals sized 8–15 nm (see Fig. 2(d)) is homogenously distributed among the glass matrix. The SAED pattern (Fig. 2(e)) and the high resolution TEM image (HRTEM, Fig. 2(f)) further reveal the crystal structure of the nanocrystal in the TEM micrograph [17].

Table 1
J–O intensity parameters ($\Omega_{2,4,6}$), calculated radiative probabilities (A), radiative lifetimes (τ_{rad}), and branching ratios (β) of Pr^{3+} ions in PGP1 and GCP1.

Transition	ν (cm^{-1})	PG			GC		
		A (S^{-1})	β	τ_{rad} (μs)	A (S^{-1})	β	τ_{rad} (μs)
$^1D_2 \rightarrow {}^3H_4$	16,595	667.96	0.25		333.68	0.25	
$^3H_5$	14,518	10.20	0.00		9.25	0.01	
$^3H_6$	12,344	183.34	0.06		180.34	0.11	
$^3F_2$	11,691	222.53	0.07		202.06	0.13	
$^3F_3$	10,300	110.54	0.04		58.78	0.04	
$^3F_4$	9867	1344.27	0.44		515.20	0.33	
$^1G_4$	6955	523.52	0.17	327	271.24	0.17	637
$^3P_0 \rightarrow {}^3H_4$	20,461	9421.63	0.31		10,200.87	0.51	
$^3H_5$	18,384	0.00	0.00		0.00	0.00	
$^3H_6$	16,210	3803.06	0.13		1557.198	0.08	
$^3F_2$	15,557	14,683.26	0.48		516.55	0.28	
$^3F_3$	14,166	0.00	0.00		0.00	0.00	
$^3F_4$	13,733	2017.24	0.07		2184.08	0.11	
$^1G_4$	10,821	345.89	0.01		374.49	0.02	
$^1D_2$	3866	60.25	0.00	33	53.92	0.00	50

Calculated J–O parameters ($\times 10^{-20}$ cm^2)	
$\Omega_2 = 5.49$	$\Omega_2 = 2.10$
$\Omega_4 = 2.66$	$\Omega_4 = 2.88$
$\Omega_6 = 5.03$	$\Omega_6 = 2.01$
$\delta_{rms} = 1.74 \times 10^{-6}$	$\delta_{rms} = 1.12 \times 10^{-6}$

3.2. Absorption spectra and J–O analysis

The absorption spectra of Pr^{3+} doped PG and GC samples are shown in Fig. 1(down). The spectra exhibit eight absorption bands centered at 2236, 1905, 1502, 998, 588, 485, 467, and 441 nm which are duly assigned to the transitions from the ground state $^3H_4$ to excited states: $^3H_2$, $^3F_2$, $^3F_{3,4}$, $^1G_4$, $^1D_2$, $^3P_0$, $^3P_1$, and $^3P_2$, respectively. It is worth noting that there are no any apparent changes in peak positions of Pr^{3+} after thermal treatment. As shown in the inset of Fig. 1, all the obtained GC samples still remain high transparency as a result of the smaller size of precipitated CaF_2 crystals than the wavelength of visible light. Hence, the scattering loss resulted from the crystallite might be negligible.

Based on the absorption spectra, J-O intensity parameters for Pr^{3+} can be derived from a least-square fitting of experimental and calculated electric dipole oscillator strengths [25,26]. The obtained values of J–O parameters Ω_t (t = 2, 4, 6) are summarized in Table 1. In general, J–O intensity parameters reflect the local structure and bonding in the vicinity of RE ions. For instance, Ω_2, it is sensitive to the ligand symmetry of the RE ions as well as the nature of bonding between RE ions and the ligand anions. The decrease of Ω_2 is usually associated with the increase in ligand symmetry surrounding RE ions and a more ionic ligand field around RE ions [27–29]. As shown in Table 1, the value of Ω_2 in GC is much smaller than that in PG, indicative of the change of local structure surrounding Pr^{3+} due to the incorporation of RE ions into CaF_2 nanocrystals after crystallization [30,31]. Once the J–O parameters have been determined, the radiative transition probability of $aJ \rightarrow bJ'$ transition, $A(aJ; bJ')$ can be obtained by the following relation:

$$A(aJ;bJ') = A_{ed} + A_{md} = \frac{64\pi^4\nu^3}{3h(2J+1)}\left[\frac{n(n^2+2)^2}{9}S_{ed} + n^3 S_{md}\right] \quad (1)$$

where ν is the energy of transition in cm^{-1} between the two multiplets, h is the Planck constant, n is the refractive index of the medium, the electric-dipole line strengths S_{ed} and magnetic-dipole

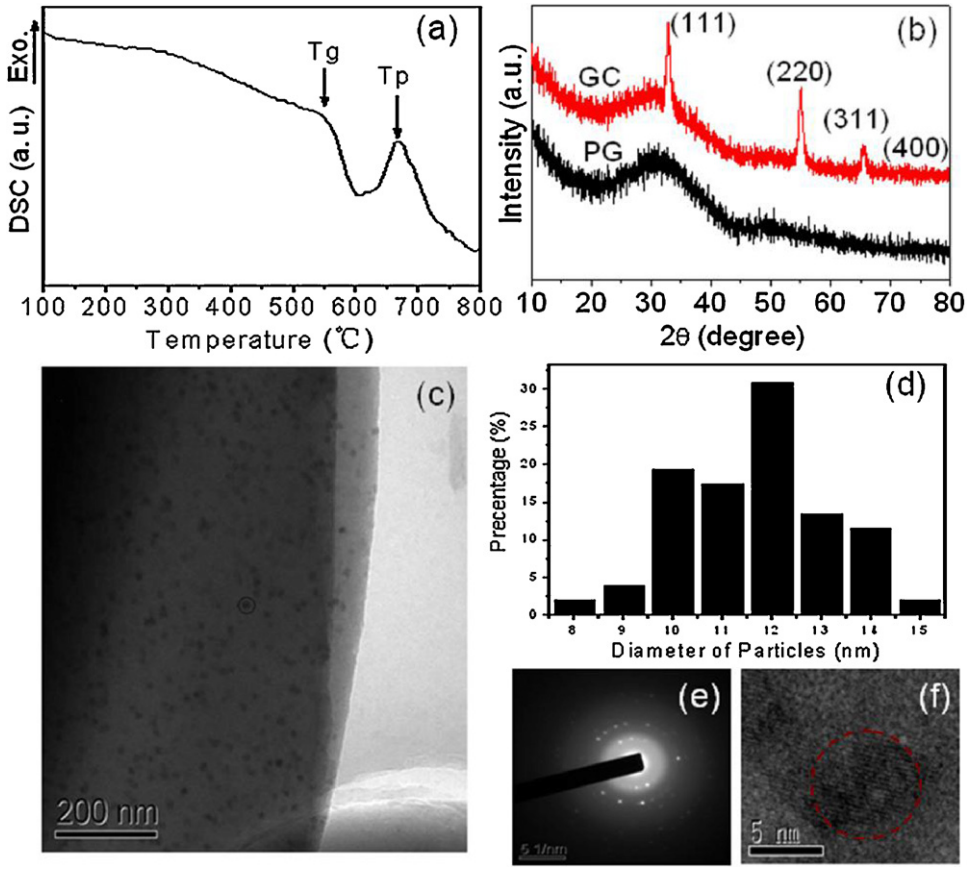

Fig. 2. (a) DSC curve of PG, T_g and T_p are glass transition and crystallization temperatures, respectively. (b) XRD patterns of PG and GC heat-treated at 570 °C for 2 h, (c) TEM micrograph of GC, (d) the size distribution of CaF_2 nanocrystals embedded in glass matrix, (e) the SAED pattern and (f) HRTEM image taken from the circle region of the TEM micrograph.

line strengths S_{md} for the states which meet the rules $\Delta S = \Delta L = 0$, $\Delta J = 0, \pm 1$ can be determined by the following expressions, respectively.

$$S_{ed}(aJ; bJ') = e^2 \sum \Omega_t |\langle aJ|U^{(t)}|bJ'\rangle^2 \quad (2)$$

$$S_{md} = \frac{e^2}{4m^2c^2}|\langle aJ|L + 2S|bJ'\rangle|^2 \quad (3)$$

where m and e are the electron mass and charge, the reduced matrix elements $U^{(t)}$ is given by Ref. [27]. The branching ratio of a transition $\beta(aJ; bJ')$ can be calculated from:

$$\beta(aJ; bJ') = \frac{A(aJ; bJ')}{\sum A(aJ; bJ')} \quad (4)$$

The radiative lifetime of an emitting state can be estimated by:

$$\tau_{rad} = \frac{1}{\sum A(aJ; bJ')} \quad (5)$$

where the sum includes all the states below aJ state. The results of A, β, τ_{rad} are also presented in Table 1.

3.3. Down-conversion luminescence in Pr^{3+}–Yb^{3+} codoped GCs

Fig. 3 presents the PL spectra of Pr^{3+} doped GC samples under 470 nm excitation. As indexed in the energy-level diagram (inset of Fig. 3), the observed emission bands can be assigned to the $^3P_0 \rightarrow {}^3H_6$, $^3P_0 \rightarrow {}^3F_2$, $_{3,4}$,$^3P_1 \rightarrow {}^1G_4$, $^1D_2 \rightarrow {}^3H_5$, and $^1D_2 \rightarrow {}^3F_4$ transitions of Pr^{3+}, respectively. The obvious 1037 nm emission originated from the transition of $^1D_2 \rightarrow {}^3F_4$ suggests the efficient population of $^1D_2$ level, and is dominate relaxation process of $^1D_2$ which has a larger branching ratio as shown in Table 1. Meanwhile, an onset of decrease in the intensity is observed for Pr^{3+} contents above 0.5 mol%. The possible ET routes among Pr^{3+} can be proposed by considering the simplified energy-level diagram in the inset of Fig. 3. Upon excitation at 470 nm, Pr^{3+} ion is firstly excited from the ground state to $^3P_1$ state, followed by radiative transition of $^3P_1 \rightarrow {}^1G_4$ generating the 872 nm emission. It is also

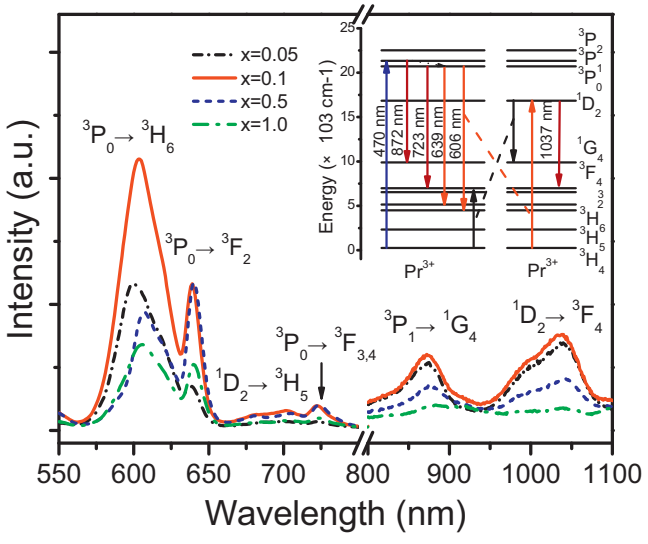

Fig. 3. Visible–NIR PL spectra of GCPx under 470 nm excitation. The inset is the simplified energy-level diagram of Pr^{3+} ions and the mechanism of ET.

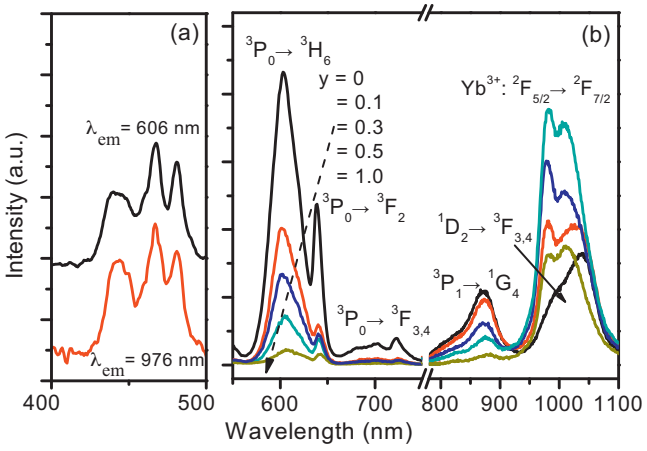

Fig. 4. (a) PLE spectra of the Pr^{3+}:$^3P_0 \rightarrow {}^3H_6$ emission in the Pr^{3+} single doped GC and the Yb^{3+}:$^2F_{5/2} \rightarrow {}^2F_{7/2}$ emission in the Pr^{3+}–Yb^{3+} codoped GC. (b) The dependence of visible–NIR PL spectra on Yb^{3+} concentration in GCY*y* samples under 470 nm excitation.

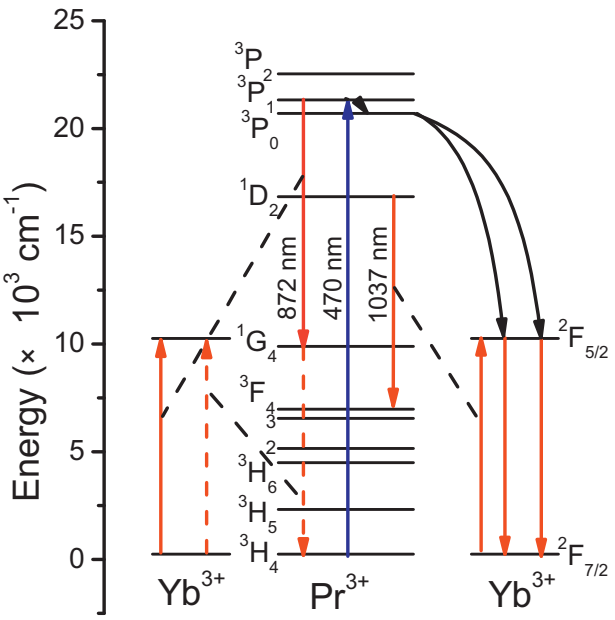

Fig. 5. Simplified energy-level diagram for the Pr^{3+}–Yb^{3+} couple, showing possible downconversion luminescence mechanism under 470 nm excitation.

possible that some of the excited Pr^{3+} ions in $^3P_1$ state undergo fast nonradiative relaxation down to the $^3P_0$ state. Then, transitions of $^3P_0 \rightarrow {}^3H_6$, $^3P_0 \rightarrow {}^3F_2$ and $^3P_0 \rightarrow {}^3F_{3,4}$ take place, giving rise to emissions at 606 nm, 639 nm and 723 nm, respectively. It is noted that the energy gap between $^3P_0$ and $^1D_2$ levels is about 3866 cm^{-1}, which is 12 times as great as the phonon cutoff of CaF_2 nanocrystal (325 cm^{-1}) and about 4 times that of the glass matrix (~1100 cm^{-1}). Therefore, the $^1D_2$ state can be populated through the following processes: (i) multiphonon relaxation process ($^3P_0 \rightarrow {}^1D_2$) of Pr^{3+} ions resided in the glass matrix, (ii) the cross relaxation (CR) process of $^3P_0 + {}^3H_4 \rightarrow {}^3H_6 + {}^1D_2$ among Pr^{3+} ions clustered in the nanocrystals, which also accounts for the quenching of emissions from $^3P_0$ level. The CR rate of $^3P_0 + {}^3H_4 \rightarrow {}^3H_6 + {}^1D_2$ increases with increasing Pr^{3+} concentration. Simultaneously, the CR process of $^1D_2 + {}^3H_4 \rightarrow {}^1G_4 + {}^3F_4$ can also be intensified when Pr^{3+} ions are heavily doped, which induces the depopulation of $^1D_2$ state [32].

Fig. 4(a) shows the PLE spectra of GC samples detected by monitoring the Pr^{3+}:$^3P_0 \rightarrow {}^3H_6$ emission at 606 nm and the Yb^{3+}:$^2F_{5/2} \rightarrow {}^2F_{7/2}$ emission at 976 nm. It is noticed that the PLE spectrum for 976 nm emission coincides with the one for 606 nm, which consists of three intense excitation bands at 442, 470 and 481 nm due to the $^3H_4 \rightarrow {}^3P_j$ (j = 2, 1, 0) transitions of Pr^{3+}. The detection of excitation bands from Pr^{3+} in the PLE spectrum of the Yb^{3+}:$^2F_{5/2} \rightarrow {}^2F_{7/2}$ emission demonstrates the occurrence of ET from Pr^{3+} to Yb^{3+}. The dependence of visible–NIR PL spectra upon excitation of 470 nm on Yb^{3+} concentration in GCY*y* samples has been illustrated in Fig. 4(b). With the addition of Yb^{3+}, intense emission bands at 976 nm were detected in addition to the aforementioned emission bands in Pr^{3+} doped GC samples. It is noted that the emission intensity of Yb^{3+} increases almost linearly with Yb^{3+} concentration up to 0.5 mol% at the cost of Pr^{3+} emission. Significant emission quenching is observed for concentrations higher than 0.5 mol%. Compared with Pr^{3+} doped GC, the Pr^{3+}:$^1D_2 \rightarrow {}^3F_4$ emission at 1037 nm is too feeble to be identified in GCY1.0. Herein, the possible DC mechanism has been illustrated in Fig. 5. After excitation of Pr^{3+}:$^3P_1$ level by 470 nm photons, there are in general two de-excitation pathways: (i) two sequential resonant ET steps from Pr^{3+} to Yb^{3+}:Pr^{3+} ($^3P_1 \rightarrow {}^1G_4$) → Yb^{3+}:($^2F_{7/2} \rightarrow {}^2F_{5/2}$) and Pr^{3+} ($^1G_4 \rightarrow {}^3H_4$) → Yb^{3+}:($^2F_{7/2} \rightarrow {}^2F_{5/2}$); (ii) a cooperative DC mechanism: Pr^{3+}:$^3P_0 \rightarrow Yb^{3+}$:$^2F_{5/2} + Yb^{3+}$:$^2F_{5/2}$. Based on the energy-matching relationship of Pr^{3+} and Yb^{3+} levels, i.e., Pr^{3+}:$^3P_0$ level lies at approximately twice the energy of Yb^{3+}:$^2F_{5/2}$ level. Subsequently, the radiative transition of Yb^{3+}:$^2F_{5/2} \rightarrow {}^2F_{7/2}$ occurs, generating two 976 nm photons. We try to figure out which DC process is more important, there are some studies pointed out that the two sequential resonant ET is four or five orders of magnitude more effective than the cooperative ET process [10,33]. However, the absence of Pr^{3+}:$^3P_0 \rightarrow {}^1G_4$ emission at 950 nm in this system indicates that the cooperative ET process should not be neglected. For GCY1.0 sample, the quenching of 1037 nm emission could be attributed to the CR process: Pr^{3+}:$^1D_2 + Yb^{3+}$:$^2F_{7/2} \rightarrow Pr^{3+}$:$^3F_4 + Yb^{3+}$:$^2F_{5/2}$, which favors 976 nm emission of Yb^{3+}.

The decay curves of the Pr^{3+}:$^3P_0 \rightarrow {}^3H_6$ emission have been plotted for GC samples doped with a fixed Pr^{3+} content of 0.1 mol% and various Yb^{3+} contents, as shown in Fig. 6. For Pr^{3+} doped GC (GCP0.1), the decay curve exhibits a near single-exponential feature, and the fluorescence lifetime of Pr^{3+}:$^3P_0$ level is determined to be 166 μs. When Yb^{3+} content beyond 1.0 mol%, the decay curves become non-exponential, and the lifetime decline

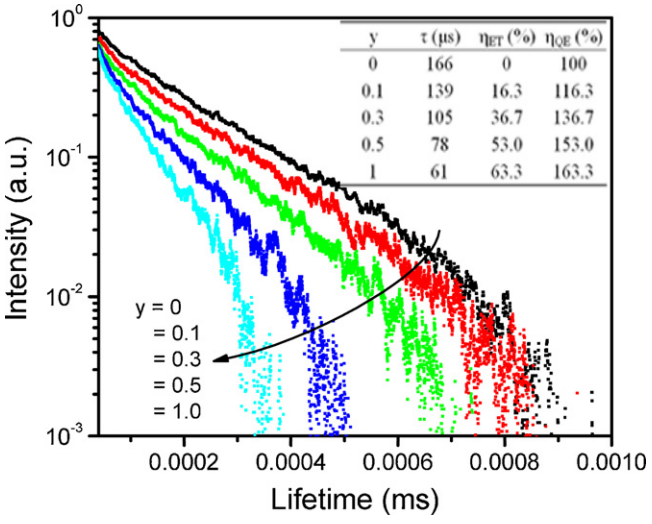

Fig. 6. Decay curves of the Pr^{3+}:$^3P_0 \rightarrow {}^3H_6$ transition in GCY*y* samples under 470 nm excitation. The inset shows ET efficiency and decay lifetime as a function of Yb^{3+} concentration.

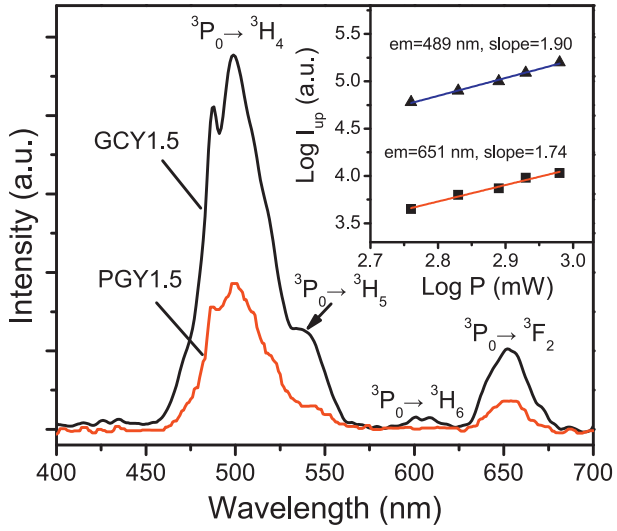

Fig. 7. Visible upconversion emission spectra of PGY1.5 and GCY1.5 under 980 nm excitation (pumping power: 2 W). The inset exhibits the log-log plot of the integrated upconversion emission intensities at 489 and 651 nm as a function of pump power at 980 nm in GCY1.5.

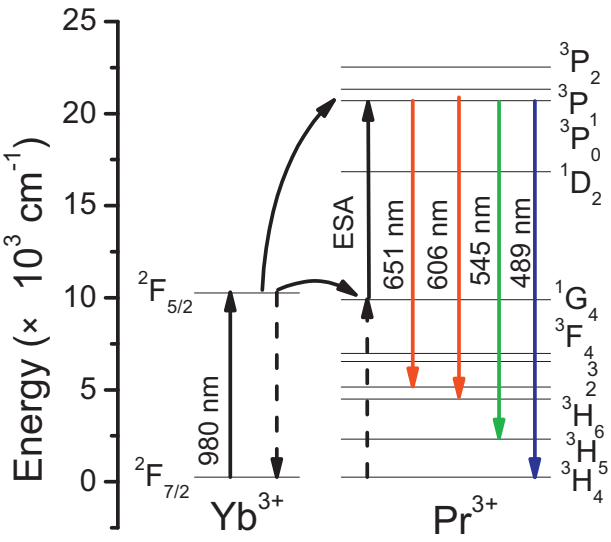

Fig. 8. Simplified energy-level diagram for Yb^{3+}–Pr^{3+} ions system, showing the possible upconversion luminescence mechanism under 980 nm excitation.

to 61 μs rapidly. This can be attributed to the presence of extra decay pathways, i.e., ET from Pr^{3+} to Yb^{3+}, which facilitates the depopulation of Pr^{3+}:$^3P_0$ state. Based on the decay curves, one can calculate the ET efficiency (η_{ET}) and the total quantum (QE) efficiency (η_{QE}) from Pr^{3+}:$^3P_0$ to Yb^{3+}:$^2F_{5/2}$ via the following expressions [34,35]: (1) $\eta_{ET,x\%Yb} = 1 - \int I_{x\%Yb}dt / \int I_{0\%Yb}dt$ and (2) $\eta_{QE} = \eta_{Pr}(1 - \eta_{ET,x\%Yb}) + 2\eta_{ET,x\%Yb}$, where $I_{x\%Yb}$ denotes the decay intensity at Yb^{3+} content of x% and η_{Pr} is set to 1. The values of η_{ET} and η_{QE} are exhibited in the inset of Fig. 6. It is noted that the η_{ET} from Pr^{3+}:$^3P_0$ to Yb^{3+}:$^2F_{5/2}$ increases up to 63.3% for the sample doped with 1 mol% Yb^{3+}. Since concentration quenching is observed at Yb^{3+} concentration of 0.5 mol%, the exact maximum QE should be 153%.

3.4. Up-conversion luminescence of Pr^{3+}–Yb^{3+} codoped GC under 980 nm excitation

Fig. 7 shows the UC emission spectra of Pr^{3+} in PGY1.5 and GCY1.5 under laser irradiation of 2 W at 980 nm. The spectra consist of four bands centered at 489, 545, 606, and 651 nm, corresponding to the respective $^3P_0 \rightarrow {}^3H_4$, $^3P_0 \rightarrow {}^3H_5$, $^3P_0 \rightarrow {}^3H_6$ and $^3P_0 \rightarrow {}^3F_2$ transitions. It is noted that the emission bands of GC are significantly intensified as compared with those of PG, which can be attributed to the reduced multiphonon relaxation probability benefited from low phonon energy environment of CaF_2 nanocrystals (325 cm^{-1}) [36]. This can be coincident with the theoretical calculation of longer lifetime of $^3P_0$ shown in Table 1. To reveal the UC mechanism, the dependence of UC emission intensity on pump power at 980 nm has been examined, as shown in the inset of Fig. 7. It is noticed that the blue (489 nm) and red (651 nm) emission signals exhibit approximately a quadratic power-law behavior on the excitation power. The slopes of fitting lines are 1.90 and 1.74, respectively, indicating that a two-pump photons process is responsible for the population of Pr^{3+}:$^3P_0$ emitting level. Herein, the possible UC mechanism is proposed, as depicted in Fig. 8. Upon excitation at 980 nm, Yb^{3+} is firstly excited from the ground state to $^2F_{5/2}$ state, followed by non-resonant ET to the neighboring Pr^{3+}:$^1G_4$ state. Subsequently, Pr^{3+} ion can be further excited to $^3P_0$ level after absorption of a second laser photon. Finally, the excited Pr^{3+} ion in $^3P_0$ level radiatively demotes to the $^3H_4$, $^3H_5$, $^3H_6$, and $^3F_2$ states, yielding the UC emissions at 489, 545, 606, and 651 nm, respectively.

4. Conclusions

In summary, we have investigated DC and UC processes of Pr^{3+}–Yb^{3+} codoped transparent oxyfluoride GCs. Upon 470 nm excitation, Pr^{3+} doped GCs yield intense visible–NIR luminescence corresponding to the $^3P_0 \rightarrow {}^3H_6$, $^3P_0 \rightarrow {}^3F_2$, $_{3,4}$, $^3P_1 \rightarrow {}^1G_4$, $^1D_2 \rightarrow {}^3H_5$, and $^1D_2 \rightarrow {}^3F_{\ 4}$ transitions, respectively. An onset of decrease in the intensity is observed for the Pr^{3+} contents beyond 0.5 mol%. For Pr^{3+}–Yb^{3+} codoped GCs, the emission intensity of Yb^{3+}:$^2F_{5/2} \rightarrow {}^2F_{7/2}$ is found to increase almost linearly with Yb^{3+} concentration up to 0.5 mol%, due to efficient ET from Pr^{3+} to Yb^{3+}. Population of Yb^{3+}:$^2F_{5/2}$ could be accomplished by cooperative ET process of Pr^{3+}:$^3P_0 \rightarrow 2Yb^{3+}$:$^2F_{5/2}$ and CR processes of Pr^{3+}:$^1D_2 + Yb^{3+}$:$^2F_{7/2} \rightarrow Pr^{3+}$:$^3F_4 + Yb^{3+}$:$^2F_{5/2}$ and Pr^{3+}:$^3P_1$ $+Yb^{3+}$:$^2F_{7/2} \rightarrow Pr^{3+}$:$^1G_4 + Yb^{3+}$:$^2F_{5/2}$. The maximum QE from Pr^{3+}:$^3P_0$ to Yb^{3+}:$^2F_{5/2}$ is calculated to be 153%. In comparison, intense UC emissions at 489, 545, 606, and 651 nm have been observed in Pr^{3+}–Yb^{3+} codoped glass and GC samples under 980 nm excitation, which is ascribed to be two-photon involved ET from Yb^{3+} to Pr^{3+}.

Acknowledgements

This work is financially supported by NSFC (Grant Nos. 51125005 and U0934001), Department of Education of Guangdong Province (Grant No. cxzd1011), and the Fundamental Research Funds for the Central Universities, SCUT.

References

[1] A. Goetzberger, C. Hebling, H.W. Schock, Mater. Sci. Eng. R. 40 (2003) 1.
[2] B. van der Zwaan, A. Rabl, Sol. Energy 74 (2003) 19.
[3] B.M. van der Ende, L. Aarts, A. Meijerink, Phys. Chem. Chem. Phys. 11 (2009) 11081.
[4] Q.Y. Zhang, X.Y. Huang, Prog. Mater. Sci. 55 (2010) 353.
[5] D. Timmerman, I. Izeddin, P. Stallinga, I.N. Yassievich, T. Gregorkiewicz, Nat. Photonics 2 (2008) 105.
[6] T. Trupke, M.A. Green, P. Würfel, J. Appl. Phys. 92 (2002) 1668.
[7] http://rredc.nrel.gov/solar/spectra/am1.5/#about.
[8] M. Peng, L. Wondraczek, J. Mater. Chem. 19 (2009) 627.
[9] Q.Y. Zhang, C.H. Yang, Z.H. Jiang, Appl. Phys. Lett. 90 (2007) 06191.

[10] D. Serrano, A. Braud, J.-L. Doualan, P. Camy, A. Benayad, V. Ménard, R. Moncorgé, Opt. Mater. 33 (2011) 1028.
[11] G. Lin, F.F. Luo, H.H. Pan, Q.X. Chen, D.P. Chen, J.R. Qiu, Q.Z. Zhao, J. Alloys Compd. 509 (2011) 6462.
[12] H. Lin, D.Q. Chen, Y.L. Yu, Z.F. Shan, P. Huang, Y.S. Wang, J. Alloys Compd. 509 (2011) 3363.
[13] J. de Wild, A. Meijerink, J.K. Rath, W.G.J.H.M. van Sark, R.E.I. Schropp, Sol. Energy Mater. Sol. Cells 94 (2010) 1919.
[14] B.M. van der Ende, L. Aarts, A. Meijerink, Adv. Mater. 21 (2009) 3073.
[15] R. Naccache, F. Vetrone, A. Speghini, M. Bettinelli, J.A. Capobianco, J. Phys. Chem. C 112 (2008) 7750.
[16] R.X. Yan, Y.D. Li, Adv. Funct. Mater. 15 (2005) 763.
[17] Q.J. Chen, W.J. Zhang, Q. Qian, Z.M. Yang, Q.Y. Zhang, J. Appl. Phys. 107 (2010) 0893511.
[18] D.C. Yu, X.Y. Huang, S. Ye, Q.Y. Zhang, J. Alloys Compd. 509 (2011) 9919.
[19] Y. Wang, J. Ohwaki, Appl. Phys. Lett. 63 (1993) 3268.
[20] G. Dantelle, M. Mortier, D. Vivien, G. Patriarche, Opt. Mater. 28 (2006) 638.
[21] Y. Xu, X. Zhang, S. Dai, B. Fan, H.L. Ma, J.L. Adam, J. Ren, G.R. Chen, J. Phys. Chem. C 115 (2011) 13056.
[22] S.J. Zeng, G.Z. Ren, C.F. Xu, J. Alloys Compd. 509 (2011) 2540.
[23] Z.Y. Lin, X.L. Liang, O. YW, C.X. Fan, S.L. Yuan, H.D. Zeng, G.R. Chen, J. Alloys Compd. 496 (2010) L33.
[24] P.A. Tick, N.F. Borrelli, I.M. Reaney, Opt. Mater. 15 (2000) 81.
[25] B.R. Judd, Phys. Rev. 127 (1962) 750.
[26] G.S. Ofelt, J. Chem. Phys. 37 (1962) 511.
[27] S. Tanabe, T. Ohyagi, N. Soga, T. Hannada, Phys. Rev. B 46 (1992) 3305.
[28] X. Zou, T. Izumitani, J. Non-Cryst. Solids 162 (1993) 68.
[29] E.W.J.L. Oomen, A.M.A. Van Dongen, J. Non-Cryst Solids 111 (1989) 205.
[30] X. Qiao, X. Fan, M. Wang, X. Zhang, Opt. Mater. 27 (2004) 597.
[31] W.J. Zhang, Q.Y. Zhang, Q.J. Chen, Q. Qian, Z.M. Yang, J.R. Qiu, P. Huang, Y.S. Wang, Opt. Express 17 (2009) 20952.
[32] H.T. Chen, R. Lian, M. Yin, L. Lou, W.P. Zhang, S.D. Xia, J.C. Krupa, J. Phys.: Condens. Matter. 13 (2001) 1151.
[33] F. Auzel, Chem. Rev. 104 (2004) 139.
[34] W.T. Wegh, H. Donker, K.D. Oskam, A. Meijerink, Science 283 (1999) 663.
[35] P. Vergeer, T.J.H. Vlugt, M.H.F. Kox, M.I. Den Hertog, J.P.J.M. van der Eerden, A. Meijerink, Phys. Rev. B 71 (2005) 014119.
[36] M. Mortier, A. Bensalah, G. Dantelle, Opt. Mater. 29 (2007) 1263.